Transition-Metal Pentatelluride ZrTe₅ and HfTe₅: A Paradigm for Large-Gap Quantum Spin Hall Insulators

Hongming Weng,[1,2] Xi Dai,[1,2,*] and Zhong Fang[1,2,†]

[1]*Beijing National Laboratory for Condensed Matter Physics, and Institute of Physics,
Chinese Academy of Sciences, Beijing 100190, China*
[2]*Collaborative Innovation Center of Quantum Matter, Beijing 100190, China*

Quantum spin Hall (QSH) insulators, a new class of quantum matter, can support topologically protected helical edge modes inside a bulk insulating gap, which can lead to dissipationless transport. A major obstacle to reaching a wide application of QSH is the lack of suitable QSH compounds, which should be easily fabricated and have a large bulk gap. Here, we predict that single-layer ZrTe₅ and HfTe₅ are the most promising candidates for large-gap insulators, with a bulk direct (indirect) band gap as large as 0.4 eV (0.1 eV) and which are robust against external strains. The three-dimensional crystals of these two materials are good layered compounds with very weak interlayer bonding, and they are located near the phase boundary between weak and strong topological insulators, paving a new way for future experimental studies on both the QSH effect and topological phase transitions.

      Subject Areas: Condensed Matter Physics, Topological Insulators

I. INTRODUCTION

A topological insulator (TI) [1,2] can support gapless boundary states inside a bulk insulating gap, which are topologically protected and robust against perturbations. Particularly in two-dimensional (2D) TIs, namely, the quantum spin Hall (QSH) insulators [3,4], the low-energy (back) scattering of the edge states is prohibited by the time-reversal symmetry, leading to the dissipationless transport edge channels and the QSH effect [5]. However, the known experimental verifications of the QSH effect in HgTe/CdTe [6] and InAs/GaSb [7] quantum-well structures require extreme conditions, such as the precisely controlled molecular-beam epitaxy (MBE) and the ultralow temperature due to the small bulk band gap of the order of meV, which greatly obstructs further experimental studies and possible applications.

To be a "good" QSH insulator, the material must meet the following important criteria: (1) It must be a good layered material to easily obtain the chemically stable 2D system; (2) it must have a large 2D bulk band gap to realize the QSH effect at high temperatures. The first proposal of graphene as a QSH insulator [3] is practically useless because of its extremely small gap (10^{-3} meV) induced by spin-orbit coupling (SOC) [8], although, so far, graphene is the best 2D material and that be easily made even by the

scotch-tape method [9]. Recently, Bi_2TeI has been proposed as another candidate for a QSH insulator [10], but its energy gap is also small. The bismuth (111) bilayer is potentially a large-gap (about 0.2 eV) QSH insulator [11]. However, its interlayer bonding is strong, and its fabrication is difficult [12]. Several other proposals, such as ultrathin tin films [13] and the Cd_3As_2 quantum well [14], have the same problem. Since they are not layered materials, the well-controlled MBE technique is required to obtain the ultrathin-film samples.

Here, we report that the simple binary compounds ZrTe₅ and HfTe₅, previously known as layered thermoelectric materials, are interlayer weakly bonded materials comparable to graphite. Their single-layer sheets, which can be made, in principle, without MBE, are QSH insulators with a large bulk gap, and they are robust against lattice distortions. Therefore, ZrTe₅ and HfTe₅ are the most promising 2D TIs that satisfy both of the above conditions and pave a new way for further experimental studies on the QSH effect. Moreover, our calculations show that the three-dimensional (3D) crystals formed by the stacking of layers are located in the vicinity of a transition between strong and weak TI, further making them a perfect platform to study the topological quantum-phase transitions.

II. COMPUTATIONAL METHODS

The *ab initio* calculations have been done by using the all-electron full-potential linearized augmented plane-wave method implemented in the WIEN2k package [15] within the general gradient approximation (GGA). The parameters used in the calculations, such as sampling of the Brillouin zone and the cutoff of augmented plane waves, are carefully

*daix@aphy.iphy.ac.cn
†zfang@aphy.iphy.ac.cn

checked to ensure the convergence. The SOC is included self-consistently within the second variational method. The interlayer binding energy, i.e., the unit-area total-energy difference between the single-layer sheet and the 3D bulk [16], is calculated by using the local-density approximation (LDA) of Perdew- and Wang-type exchange correlation [17]. The maximally localized Wannier functions (MLWF) for Te p orbitals have been constructed by using a home-made code [18] based on OpenMX [19], which can reproduce the band structures calculated from the first principles quite well. The surface and edge states have been calculated for slabs by using a tight-binding model constructed from the MLWFs generated above.

III. RESULTS

A. Layered crystal structure

Both $ZrTe_5$ and $HfTe_5$ take the same crystal structure and have very similar properties. They have been shown to possess interesting electrical-transport properties, such as the giant resistivity anomaly [20,21] and large thermopower [22,23]. They crystallize in the orthorhombic layered structure [24] with space group $Cmcm$ (D_{2h}^{17}), as shown in Fig. 1 (hereafter, we take $ZrTe_5$ as an example). Trigonal prismatic chains of $ZrTe_3$ (marked by a red dashed line) run along the a axis, and these prismatic chains are linked via parallel zigzag chains of Te atoms along the c axis to form a
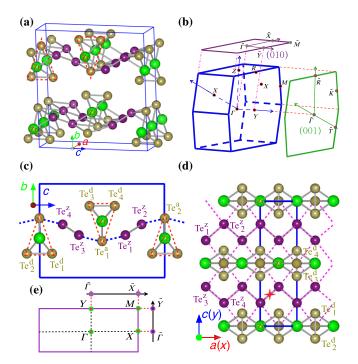

FIG. 2 (color online).   The calculated interlayer binding energies for several typical layered compounds.

2D sheet of $ZrTe_5$ in the a-c plane. The sheets of $ZrTe_5$ stack along the b axis, forming a layered structure. The prism of $ZrTe_3$ is formed by a dimer of $Te_{1,2}^d$ atoms (with the superscript d indicating the dimer and the subscript 1, 2 numbering the atoms) and one apical Te^a atom (with a meaning the apical), while the zigzag chain is formed by two $Te_{1,2}^z$ atoms (with z indicating the zigzag chain). The primitive unit cell contains two formula units with two prismatic chains and two zigzag chains. The corresponding subscripts numbering the atoms should be doubled.

$ZrTe_5$ shows strong quasi-2D anisotropy [25]. The prismatic and the zigzag chains are connected through the apical Te atoms, and the Te-Te bond length between two chains is about 0.4 Å longer than that in the zigzag chain. If the Zr and Te^d dimer atoms are neglected, the remaining apical Te^a and zigzag Te^z atoms can be viewed as a waved grid of Te square-lattice sheet [see Fig. 1(d)], leading to a stable quasi-2D structure. Each $ZrTe_5$ layer is nominally charge neutral, and the interlayer distance (along the b axis) is quite large (about 7.25 Å), suggesting the weak interlayer coupling, presumably of van der Waals type. We have calculated the interlayer binding energies for different compounds by using the first-principles total energy method (see Sec. II). The results shown in Fig. 2 suggest that the interlayer binding energy of $ZrTe_5$ or $HfTe_5$ is as weak as that of graphite and is much smaller than that of the Bi_2Se_3 and Bi (111) bilayers. Given the easy procedure of making graphene from graphite simply by exfoliation with scotch tape [9], the comparably weak interlayer binding energy suggests that a single layer of $ZrTe_5$ (or $HfTe_5$) may be formed in a similar simple and efficient way.

B. 2D quantum spin Hall insulator

We now focus on the single layer of $ZrTe_5$ in the a-c plane. Its structure is fully optimized by theoretical calculations. It is found that the relaxed lattice constants ($a = 4.036$ Å and $c = 13.843$ Å) and the internal atomic coordinates are all very close to their 3D bulk experimental values (less than 1% difference) [24], again suggesting the stability of the single-layer sheet. The calculated density of states shown in Fig. 3(a) suggests that the Zr-4d states are

FIG. 1 (color online).   (a) The crystal structure. (b) The bulk Brillouin zone (BZ) and the projected surface BZ of 3D $ZrTe_5$ ($HfTe_5$). (c), (d), and (e) The side view, top view, and BZ of the single-layer structure, respectively. In (d), the inversion center is indicated by the red star symbol, and the waved grid of the Te square lattice sheet is shown by the pink dotted lines.
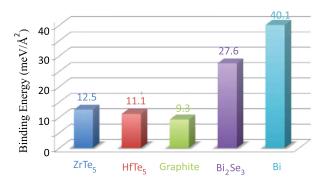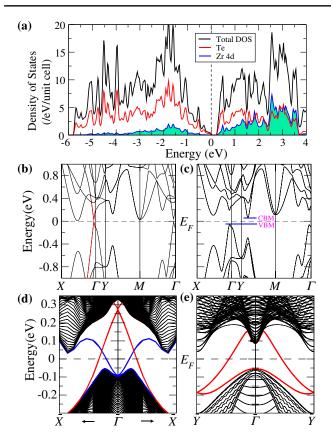
FIG. 3 (color online). The calculated electronic structures of single-layer ZrTe$_5$. (a) The density of states. (b) and (c) The band structures without and with SOC, respectively. The valence-band maximum (VBM) and conduction-band minimum (CBM) defining the indirect band gap are indicated in (c). (d) and (e) The calculated edge states for the x and y edges, respectively (see the main text for details).

mostly unoccupied above the Fermi level, leading to the nearly ionic Zr^{4+} state (by transferring about four electrons onto the neighboring Te atoms). The states near the Fermi level are dominantly from the covalently bonded Te-5p states.

For the convenience of discussion, hereafter we define our coordinate system with x, y being along the a and c axes, respectively, and z being out of the 2D plane. We choose the origin of the coordinate system to be located on the Zr site. The calculated band structures for a single-layer ZrTe$_5$ are shown in Figs. 3(b) and 3(c). In the case without SOC, the system is a semimetal with one band crossing along the Γ-X direction, implying the existence of band inversion around Γ-X. The band crossing is unavoidable because the two bands belong to different representations distinguished by the mirror symmetry m_{xz} (the mirror plane is parallel to the xz plane and passes through the Zr site) along the Γ-X axis. The inclusion of SOC will, however, mix them and open up a gap, resulting in an insulator with a large direct (indirect) band gap of 0.4 eV (0.1 eV). We have investigated the Z_2 topological invariant [3] of this

insulating state by evaluating the parity eigenvalues of occupied states at four time-reversal-invariant-momentum (TRIM) points of the BZ [26], and we have concluded that it is a nontrivial QSH insulator with $Z_2 = 1$. Since the band gap is mostly determined by the SOC strength of Te p orbitals, we do not expect much of an error bar of GGA-type calculations (as is usual for conventional semiconductors). Indeed, we have checked the electronic structure by using the hybrid functional HSE06 [27], as well as the modified Becke-Johnson (mBJ) potential [28]. Both of them give a similar band gap with the band topology unchanged since the band gap is opened by SOC between bonding and antibonding states of Te p orbitals with very weak correlation effects.

The 2D nontrivial insulating state in single-layer ZrTe$_5$ should support topologically protected conducting edge states. They are calculated by using the slab model constructed with the tight-binding method (see Method). For slab cutting along the x direction, one side is terminated with a ZrTe$_3$ prismatic chain and the other side with a Te zigzag chain (see Fig. 7 in Appendix A).This asymmetric slab leads to two separated Dirac cones at $\bar{\Gamma}$, as shown in Fig. 3(d). The red lines show the edge with prismatic chain termination, and the blue lines show the zigzag chain termination. For the slab cutting along the y axis, the two edges are the same. This symmetric slab model leads to two energetically degenerate Dirac cones located at opposite sides. Because of the nontrivial topology, the edge states always exist, while their details may depend explicitly on the edge; for example, the Dirac cones are located at the $\bar{\Gamma}$ point for the x edge but at the $\bar{Y}$ point for the y edge.

C. Band inversion mechanism

The band inversion in single-layer ZrTe$_5$ is not due to SOC; instead, it is mainly due to the nonsymmorphic features of the space group. Therefore, the physics of band inversion here can be understood without SOC, and the only effect of SOC is to open up an energy gap afterwards. We note that the space group of the single-layer ZrTe$_5$ is P_{mmn} (D_{2h}^{13}), which is nonsymmorphic, with the inversion center located not at the origin but at (1/4, 1/4). As an important consequence of such space group symmetry, all of the eigenstates at the zone-boundary TRIM points [namely, X, Y, and M in Fig. 1(e)] are fourfold degenerate (including the spin degree of freedom), with two of them having even parity and the other two odd parity. This is because at the three zone boundary points, the inversion operation anticommutes with two important mirror operators, m_{xz} and m_{yz} (see the Appendix B for details). The equal number of bands with odd and even parity guarantees that any band inversion at those zone-boundary TRIM points will not change the topology of the system, and the Z_2 index of the material is fully determined by the energy order of the bands at the Γ point, where only the Kramer degeneracy holds. We further notice that the mirror
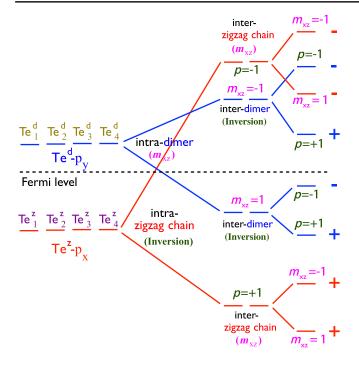
FIG. 4 (color online).   The schematic illustration of the band inversion mechanism (see main text for details).

symmetry m_{yz} will transfer all the atoms into themselves. Therefore, the atomic p orbitals can be classified into two classes, namely, the p_x orbital and the $p_{y/z}$ orbital, because they will not mix in the eigenstates of the Γ point (in the absence of SOC).

Our calculations suggest that the band inversion at Γ happens between the zigzag chain Te^z-p_x and the prism chain dimer Te^z-p_y states, as shown schematically in Fig. 4. At the atomic limit, they are all fourfold degenerate since there are four equivalent Te atoms for each class. The strong intrachain covalent bonding will split them into doubly degenerate bonding and antibonding states, respectively, and then the weak interchain coupling will further split them into singly degenerate states. It is important to note the symmetry difference between the two chains. The two dimer $Te^d_{1,2}$ atoms in the same prism chain are related mirror m_{xz} symmetry, while the two $Te^d_{1,2}$ atoms in the same zigzag chain are related by inversion symmetry. As a result, the bonding and antibonding states formed by intrachain coupling can be distinguished by the eigenvalues $m_{xz} = \pm 1$ for the former and the parity $p = \pm 1$ for the latter. Because of the strong intrachain coupling, the band inversion is introduced between the bonding Te^d states with $m_{xz} = 1$ and the antibonding Te^z states with $p = -1$, as illustrated in Fig. 4. Within the two bonding Te^d states of $m_{xz} = 1$, only one state has odd parity. As a result, its occupation changes the total parity of the occupied states at Γ, which leads to the QSH state. The apical Te^d atoms do not contribute to the band inversion because their bonding-antibonding separation of p orbitals is smaller (because of the larger atomic distance), and the bonding

and antibonding states are always occupied or unoccupied simultaneously.

D. Strain effects

We emphasize that, unlike the situation in typical TI such as the Bi_2Se_3 family compounds [29], the band inversion in single-layer $ZrTe_5$ is not due to SOC; instead, it is due to the special nonsymmorphic space group features, as discussed above. As long as the interchain coupling is not strong enough to reverse the band ordering again [between the ($m_{xz} = -1$, $p = +1$) state and the ($m_{xz} = 1$, $p = -1$) state, as shown in Fig. 4], the QSH state should be stable. We have checked the stability of this QSH state as a function of lattice strain. Without loss of generality, we assume that the lattice parameters a and c are equally scaled by possible external potentials, and for each fixed volume, we fully optimize the internal atomic coordinates. The results shown in Fig. 5 suggest that the QSH state survives even if the volume is expanded by more than 20% or compressed by 10%, indicating its robust stability against the strains. This makes the QSH state highly adaptable in various application environments.In the case of compression, the over-enhanced interchain coupling will finally kill the QSH state, as discussed above.

E. 3D weak and strong TI

Given the QSH state in single-layer $ZrTe_5$, it is important to check if the stacked 3D compound is a weak or strong TI [30]. Interestingly, if we use the experimental lattice parameters [24], we get a 3D strong TI with a topological invariant (1; 001). However, if the optimized lattice parameters, which are only about 2% larger than experimental ones, are used, we get a 3D weak TI state [31] with a topological invariant (0; 001). The differences between the two solutions are from the tiny overlap of the states at
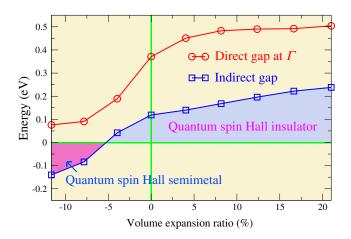

FIG. 5 (color online).   The calculated band gaps of single-layer $ZrTe_5$ as a function of volume change. Both the direct gap at Γ and the indirect band gap are shown. The nontrivial Z_2 topology survives as long as the band gap at Γ remains positive.
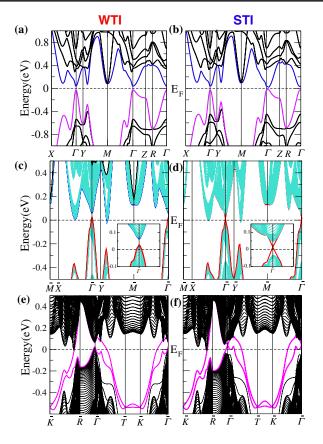
FIG. 6 (color online). The calculated band structures and surface states for 3D $ZrTe_5$. Panels (a) and (b) are for the bulk. Panels (c) and (d) are for the top surface, and panels (e) and (f) are for the side surfaces, as indicated in Fig. 1. The weak TI (WTI) solutions (left panels) are obtained by using optimized lattice parameters, while the strong TI (STI) solutions (right panels) are from the experimental ones. (See main text for details.)

the Γ point of the 3D BZ, which inverse the parity (see Fig. 6). If we use the mBJ potential [28] instead of GGA for the above two calculations, we get strong TI solutions. Our results suggest that the 3D compound is located very close to the boundary between the weak and strong TI, which provides us with an excellent opportunity to study the topological phase transition experimentally. In Fig. 6, we show the calculated band structures and the surface states of both strong and weak TI solutions. Odd numbers of Dirac cones, one for the top and three for the side surface, are obtained in the strong TI phase. For the weak TI case, however, even numbers of Dirac cones, none for the top and two for the side surface, are obtained. It will be very interesting to observe such topological phase transitions in experiments, simply by pressing or stretching the sample along the stacking direction. Considering the large magneto-resistive effect observed in both $ZrTe_5$ and $HfTe_5$ [20], it will also be heuristic to see whether the long-standing mysterious giant resistivity anomaly [21] has anything to do with the possible weak-to-strong TI phase

transition, by carefully studying the change of lattice parameters and the possible surface states as a function of temperature or pressure.

IV. DISCUSSION

We have also performed all the calculations for $HfTe_5$, and we draw the same conclusions as for $ZrTe_5$. Their 2D and 3D band structures and band-gap sizes are all very similar. The results for a single layer of $HfTe_5$ are shown in Fig. 8 in the Appendix B for comparison. We have also tried to explore more possible isoelectronic compounds, such as $TiTe_5$ and the similar selenides and sulphides. However, to the best of our knowledge, there is no experimental report of their existence as yet and they are well worth the experimental trials [32]. On the other hand, it is experimentally known that the transition metal Zr or Hf can be substituted by many other elements, such as rare earth, which even shows precursor of possible magnetic ordering [23]. The breaking of time-reversal symmetry will allow us to study the possible quantum anomalous Hall effect [33,34]. Among possible tetravalent magnetic rare-earth elements, we find that Pr^{4+} and Tb^{4+} have slightly larger ionic radii than Zr^{4+} and Hf^{4+}. They might be able to realize the isovalent substitution of Zr and Hf. Moreover, because of the strong 2D features of these materials, the edge states will appear not only at the edge of the single-layer samples but also at the terrace edges on the top surface of the 3D materials. When such terrace edges are covered by an s-wave superconducting layer, 1D topological super-conductors with Majorana bound states at the end of the terrace edges will be induced by the superconducting proximity effect [35–37].

APPENDIX A: EDGES IN SLAB MODEL AND BAND STRUCTURE OF SINGLE-LAYER HfTe$_5$

To calculate the edge states of single-layer $ZrTe_5$ along the x and y axes, we have constructed a tight-binding model Hamiltonian for the 40-unit-cell-thick slab based on the Wannier function generated for Te p orbitals. For the x edge, the slab is terminated with a Te zig-zag chain on one side and a $ZrTe_5$ prism chain on the other side, as shown in Fig. 7(a). For the y edge, the slab is terminated with equivalent left and right edges, as shown in Fig. 7(b).

We have also performed calculations for $HfTe_5$ and found that it has nearly the same electronic structure as the $ZrTe_5$. For comparison, we show the band structure for single layer of $HfTe_5$ in Fig. 8 without and with SOC. It can easily be seen that both of them are very similar to those of
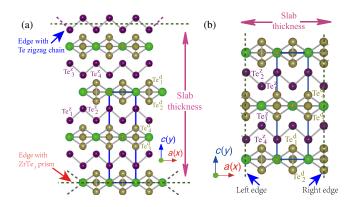
FIG. 7 (color online).　A schematic picture of the 40-unit-cell-thick slab used to calculate edges states. (a) The asymmetric slab terminated with a Te zigzag chain and a $ZrTe_3$ prism chain for the x edge. (b) The symmetric slab for the y edge.
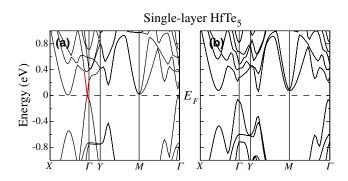

FIG. 8 (color online).　The calculated band structures of single-layer $HfTe_5$ (a) without and (b) with SOC, respectively.

$ZrTe_5$. The indirect band gap of $HfTe_5$ is slightly larger than that of $ZrTe_5$ since Hf is heavier than Zr, and Te p orbitals are hybridized with their d orbitals.

APPENDIX B: BAND PARITY AT ZONE-BOUNDARY TRIM POINTS OF THE NONSYMMORPHIC SPACE GROUP

We prove that for single-layer $ZrTe_5$ and $HfTe_5$, the energy bands at all the zone-boundary TRIM points are at least doubly degenerate with opposite parity. For simplicity, we neglect the spin degree of freedom, and the conclusion can easily be generalized to the spin-$1/2$ case. Since the energy bands of $ZrTe_5$ near the Fermi level are formed by Te $5p$ orbitals, the Wannier functions centered at each atomic site with a particular atomic feature (like p_x, p_y, and p_z) carry a natural representation for the space group. First, we define the following Wannier basis in the momentum space,

$$\varphi_{\alpha k}^{\mu}(r) = \frac{1}{\sqrt{N}} \sum_i \varphi_\alpha(r - \tau_\mu - R_i) e^{ik(R_i + \tau_\mu)},$$

where i is the unit-cell index, μ denotes the different atomic positions in a unit cell, and α labels different orbitals at the

same atomic position. When a general space group operator $\{P_R | t_R\}$, with P_R and t_R representing the rotation and translation parts of the operator, respectively, acts on the Wannier basis, we have

$$\{P_R | t_R\} \varphi_{\alpha k}^{\mu}(r) = t_R(P_R \varphi_{\alpha k}^{\mu}(r))$$
$$= \frac{1}{\sqrt{N}} \sum_{i'} \varphi_{\mathcal{R}\alpha}(r - t_{\mathcal{R}} - \mathcal{R}\tau_\mu - R_{i'})$$
$$\times e^{i(\mathcal{R}k)(R_{i'} + \mathcal{R}\tau_\mu)}$$
$$= \frac{1}{\sqrt{N}} \sum_{i'\alpha'\mu'} \varphi_{\alpha'}(r - R_0^\mu - \tau_{\mu'} - R_{i'})$$
$$\times e^{i(\mathcal{R}k)(R_{i'} + R_0^\mu + \tau_{\mu'} - t_R)}$$
$$= \varphi_{\mathcal{R}\alpha, \mathcal{R}k}^{\mu'}(r) e^{-i(\mathcal{R}k)t_R}$$
$$= \sum_{\alpha'\mu'} Z_{\mu\mu'}^{\mathcal{R}} O_{\alpha\alpha'}^{\mathcal{R}} \varphi_{\alpha', \mathcal{R}k}^{\mu'}(r) e^{-i(\mathcal{R}k)t_R},$$

where we have taken $t_R + \mathcal{R}\tau_\mu = R_0^\mu + \tau_{\mu'}$ and $\alpha' = \mathcal{R}\alpha$, and $Z^{\mathcal{R}}$ and $O^{\mathcal{R}}$ are matrices describing the transformation in atomic positions and orbitals, respectively. We emphasize that in the above equation, $\varphi_{\alpha\mathcal{R}k}^{\mu}(r)$ does not necessarily equal $\varphi_{\alpha k}^{\mu}(r)$, even when $\mathcal{R}k = k + G_n$, with G_n representing a vector in the reciprocal lattice. They can differ by a phase factor because of the specific choice of the gauge-fixing condition here, which contains a phase factor $e^{ik\tau_\mu}$ for orbitals located at different atomic positions τ_μ. Using the Wannier representation introduced above and choosing the Zr site as the origin of the coordinate frame, we pick two operators, inversion and mirror m_{yz}, which can be written as follows:

$$\left\{ I \Big| \frac{1}{2}, \frac{1}{2} \right\} \qquad \text{and} \qquad \{m_{yz} | 0, 0\}.$$

First, we apply $\{I | \frac{1}{2}, \frac{1}{2}\} \cdot \{m_{yz} | 0, 0\}$ to the Wannier basis, which leads to

$$\left\{ I \Big| \frac{1}{2}, \frac{1}{2} \right\} \cdot \{m_{yz} | 0, 0\} \varphi_{\alpha k}^{\mu}(r)$$
$$= [Z^I Z^{yz}]_{\mu\mu'} [O^I O^{yz}]_{\alpha,\alpha'} \varphi_{\alpha'(Im_{yz}k)}^{\mu'}(r) e^{-i(Im_{yz}k)t_R},$$

where we have $t_R = \{\frac{1}{2}, \frac{1}{2}\}$. And, similarly, with $\{m_{yz} | 0, 0\} \cdot \{I | \frac{1}{2}, \frac{1}{2}\}$, we have

$$\{m_{yz} | 0, 0\} \cdot \left\{ I \Big| \frac{1}{2}, \frac{1}{2} \right\} \varphi_{\alpha k}^{\mu}(r)$$
$$= [Z^{yz} Z^I]_{\mu\mu'} [O^{yz} O^I]_{\alpha,\alpha'} \varphi_{\alpha'(m_{yz}Ik)}^{\mu'}(r) e^{-i(Ik)t_R}.$$

Since we can easily prove that $Z^{yz} Z^I = Z^I Z^{yz}$ and $O^{yz} O^I = O^I O^{yz}$, the only difference between the above two formulas is the phase factor, which differs by -1 for

$(\pi, 0)$ and (π, π). Therefore, for these two points, we have $\{I|\frac{1}{2}, \frac{1}{2}\} \cdot \{m_{yz}|0,0\} = -\{m_{yz}|0,0\} \cdot \{I|\frac{1}{2}, \frac{1}{2}\}$. Because both of the above symmetry operators commute with the Hamiltonian, we can easily prove that if φ_k is an eigenstate of the Hamiltonian with a given parity, the state $\{m_{yz}|0,0\}\varphi_k$ is another eigenstate of the Hamiltonian but with opposite parity. Therefore, we have proved that at $(\pi, 0)$ and (π, π), all the states come in pairs with opposite parity. Replacing m_{yz} by another mirror m_{xz}, we can easily prove that another zone-boundary TRIM point $(0, \pi)$ has the same property. In conclusion, at all of these zone-boundary TRIM points, the eigenstates always come in degenerate pairs with opposite parity.

[1] M. Z. Hasan and C. L. Kane, *Colloquium: Topological Insulators*, Rev. Mod. Phys. **82**, 3045 (2010).

[2] X.-L. Qi and S.-C. Zhang, *Topological Insulators and Superconductors*, Rev. Mod. Phys. **83**, 1057 (2011).

[3] C. L. Kane and E. J. Mele, *Quantum Spin Hall Effect in Graphene*, Phys. Rev. Lett. **95**, 226801 (2005); $\mathbf{Z}_2$ *Topological Order and the Quantum Spin Hall Effect*, Phys. Rev. Lett. **95**, 146802 (2005).

[4] B. A. Bernevig and S. C. Zhang, *Quantum Spin Hall Effect*, Phys. Rev. Lett. **96**, 106802 (2006).

[5] B. A. Bernevig, T. L. Hughes, and S. C. Zhang, *Quantum Spin Hall Effect and Topological Phase Transition in HgTe Quantum Eells*, Science **314**, 1757 (2006).

[6] M. König, S. Wiedmann, C. Brüne, A. Roth, H. Buhmann, L. W. Molenkamp, X. L. Qi, and S. C. Zhang, *Quantum Spin Hall Insulator State in HgTe Quantum Wells*, Science **318**, 766 (2007).

[7] I. Knez, R. R. Du, and G. Sullivan, *Evidence for Helical Edge Modes in Inverted* InAs = GaSb *Quantum Wells*, Phys. Rev. Lett. **107**, 136603 (2011).

[8] Y. G. Yao, F. Ye, X. L. Qi, S. C. Zhang, and Z. Fang, *Spin-Orbit Gap of Graphene: First-Principles Calculations*, Phys. Rev. B **75**, 041401 (2007).

[9] K. S. Novoselov, A. K. Geim, S. V. Morozov, D. Jiang, Y. Zhang, S. V. Dubonos, I. V. Grigorieva, and A. A. Firsov, *Electric Field Effect in Atomically Thin Carbon Films*, Science **306**, 666 (2004); A. K. Geim and K. S. Novoselov, *The Rise of Graphene*, Nat. Mater. **6**, 183 (2007).

[10] P. Tang, B. Yan, W. Cao, S.-C. Wu, C. Felser, and W. Duan, *Weak Topological Insulators Induced by the Inter-layer Coupling: A First-Principles Study of Stacked* Bi_2TeI, arXiv:1307.8054.

[11] S. Murakami, *Quantum Spin Hall Effect and Enhanced Magnetic Response by Spin-Orbit Coupling*, Phys. Rev. Lett. **97**, 236805 (2006).

[12] T. Hirahara, G. Bihlmayer, Y. Sakamoto, M. Yamada, H. Miyazaki, S.-i. Kimura, S. Blügel, and S. Hasegawa, *Interfacing 2D and 3D Topological Insulators: Bi(111) Bilayer on* Bi_2Te_3, Phys. Rev. Lett. **107**, 166801 (2011); F. Yang, L. Miao, Z. F. Wang, M.-Y. Yao, F. Zhu, Y. R. Song, M.-X. Wang, J.-P. Xu, A. V. Fedorov, Z. Sun, G. B. Zhang, C. Liu, F. Liu, D. Qian, C. L. Gao, and J.-F. Jia, *Spatial and Energy Distribution of Topological Edge States in Single Bi(111) Bilayer*, ibid. **109**, 016801 (2012).

[13] Y. Xu, B. H. Yan, H. J. Zhang, J. Wang, G. Xu, P. Z. Tang, W. H. Duan, and S. C. Zhang, *Large-Gap Quantum Spin Hall Insulators in Tin Films*, Phys. Rev. Lett. **111**, 136804 (2013).

[14] Z. J. Wang, H. M. Weng, Q. S. Wu, X. Dai, and Z. Fang, *Three Dimensional Dirac Semimetal and Quantum Spin Hall Effect in* Cd_3As_2, Phys. Rev. B **88**, 125427 (2013).

[15] P. Blaha, K. Schwarz, G. Madsen, D. Kvasicka, and J. Luitz, *WIEN2k, An Augmented Plane Wave Plus Local Orbitals Program for Calculating Crystal Properties* (TU Vienna, Vienna, 2001).

[16] H. Lind, S. Lidin, and U. Häussermann, *Structure and Bonding Properties of* $(Bi_2Se_3)_m(Bi_2)_n$ *Stacks by First-Principles Density Functional Theory*, Phys. Rev. B **72**, 184101 (2005).

[17] J. P. Perdew and Y. Wang, *Accurate and Simple Analytic Representation of the Electron-Gas Correlation Energy*, Phys. Rev. B **45**, 13244 (1992).

[18] H. Weng, T. Ozaki, and K. Terakura, *Revisiting Magnetic Coupling in Transition-Metal-Benzene Complexes with Maximally Localized Wannier Functions*, Phys. Rev. B **79**, 235118 (2009).

[19] http://www.openmx-square.org.

[20] T. M. Tritt, N. D. Lowhorn, R. T. Littleton IV, A. Pope, C. R. Feger, and J. W. Kolis, *Large Enhancement of the Resistive Anomaly in the Pentatelluride Materials* $HfTe_5$ *and* $ZrTe_5$ *with Applied Magnetic Field*, Phys. Rev. B **60**, 7816 (1999).

[21] E. F. Skelton, T. J. Wieting, S. A. Wolf, W. W. Fuller, D. U. Gubser, T. L. Francavilla, and F. Levy, *Giant Resistivity and X-ray Diffraction Anomalies in Low-Dimensional* $ZrTe_5$ *and* $HfTe_5$, Solid State Commun. **42**, 1 (1982).

[22] W. W. Fuller, S. A. Wolf, T. J. Wieting, R. C. LaCoe, P. M. Chaikin, and C. Y. Huang, *Pressure Effects in* $HfTe_5$ *and* $ZrTe_5$, J. Phys. (Paris), Colloq. **44**, C3-1709 (1983).

[23] N. D. Lowhorn, T. M. Tritt, E. E. Abbott, and J. W. Kolis, *Enhancement of the Power Factor of the Transition Metal Pentatelluride* $HfTe_5$ *by Rare-Earth Doping*, Appl. Phys. Lett. **88**, 022101 (2006).

[24] H. Fjellvå g and A. Kjekshus, *Structural Properties of* $ZrTe_5$ *and* $HfTe_5$ *as Seen by Powder Diffraction*, Solid State Commun. **60**, 91 (1986).

[25] A. Smontara, K. Biljakovi¢, M. Miljak, and T. Sambong, *Thermal and Magnetic Measurements on* $ZrTe_5$, Physica (Amsterdam) **143B**, 267 (1986).

[26] L. Fu and C. L. Kane, *Topological Insulators with Inversion Symmetry*, Phys. Rev. B **76**, 045302 (2007).

[27] J. Heyd, G. E. Scuseria, and M. Ernzerhof, *Hybrid Functionals Based on a Screened Coulomb Potential*, J. Chem. Phys. **118**, 8207 (2003); *Hybrid Functionals Based on a Screened Coulomb Potential*, J. Chem. Phys. **124**, 219906(E) (2006).

[28] F. Tran and P. Blaha, *Accurate Band Gaps of Semiconductors and Insulators with a Semilocal Exchange-Correlation Potential*, Phys. Rev. Lett. **102**, 226401 (2009).

[29] H. J. Zhang, C.-X. Liu, X.-L. Qi, X. Dai, Z. Fang, and S.-C. Zhang, *Topological Insulators in* Bi_2Se_3, Bi_2Te_3 *and* Sb_2Te_3 *with a Single Dirac Cone on the Surface*, Nat. Phys. **5**, 438 (2009).

[30] L. Fu, C. L. Kane, and E. J. Mele, *Topological Insulators in Three Dimensions*, Phys. Rev. Lett. **98**, 106803 (2007).

[31] B. Yan, L. Müchler, and C. Felser, *Prediction of Weak Topological Insulators in Layered Semiconductors*, Phys. Rev. Lett. **109**, 116406 (2012).

[32] S. Lebègue, T. Björkman, M. Klintenberg, R. M. Nieminen, and O. Eriksson, *Two-Dimensional Materials from Data Filtering and Ab Initio Calculations*, Phys. Rev. X **3**, 031002 (2013).

[33] R. Yu, W. Zhang, H.-J. Zhang, S.-C. Zhang, X. Dai, and Z. Fang, *Quantized Anomalous Hall Effect in Magnetic Topological Insulators*, Science **329**, 61 (2010).

[34] C. Z. Chang *et al.*, *Experimental Observation of the Quantum Anomalous Hall Effect in a Magnetic Topological Insulator*, Science **340**, 167 (2013).

[35] V. Mourik, K. Zuo, S. M. Frolov, S. R. Plissard, E. P. A. M. Bakkers, and L. P. Kouwenhoven, *Signatures of Majorana Fermions in Hybrid Superconductor-Semiconductor Nanowire Devices*, Science **336**, 1003 (2012).

[36] R. M. Lutchyn, J. D. Sau, and S. Das Sarma, *Majorana Fermions and a Topological Phase Transition in Semiconductor-Superconductor Heterostructures*, Phys. Rev. Lett. **105**, 077001 (2010).

[37] Y. Oreg, G. Refael, and F. von Oppen, *Helical Liquids and Majorana Bound States in Quantum Wires*, Phys. Rev. Lett. **105**, 177002 (2010).